

Contents lists available at ScienceDirect

Science Bulletin

journal homepage: www.elsevier.com/locate/scib



Article

Implementation and topological characterization of Weyl exceptional rings in quantum-mechanical systems

Hao-Long Zhang ^{a,1}, Pei-Rong Han ^{a,b,1}, Xue-Jia Yu ^{a,1}, Shou-Bang Yang ^a, Jia-Hao Lü ^a, Wen Ning ^{a,*}, Fan Wu ^a, Qi-Ping Su ^c, Chui-Ping Yang ^c, Zhen-Biao Yang ^{a,d,*}, Shi-Biao Zheng ^{a,d,*}

ARTICLE INFO

Article history: Received 26 March 2025 Received in revised form 28 April 2025 Accepted 19 May 2025 Available online 4 June 2025

Keywords: Non-Hermitian systems Geometric and topological phase Open systems and decoherence

ABSTRACT

Non-Hermiticity can lead to the emergence of many intriguing phenomena that are absent in Hermitian systems, enabled by exceptional topological defects, among which Weyl exceptional rings (WER) are particularly interesting. The topology of a WER can be characterized by the quantized Berry phase and a nonzero Chern number, both encoded in the eigenvectors of the non-Hermitian Hamiltonian. So far, WERs have been realized with classical wave systems, whose eigenvectors can be well described by classical physics. We here report the first quantum-mechanical implementation of WERs and investigate the related topology transitions. The experiment system consists of a superconducting qubit and a dissipative resonator, coupled to each other. The high flexibility of the system enables us to characterize its eigenvectors on different manifolds of parameter space, each of which corresponds to a quantum-mechanical entangled state. We extract both the quantized Berry phase and Chern number from these eigenvectors, and demonstrate the topological transition triggered by shrinking the size of the corresponding loop or manifold in parameter space.

© 2025 Science China Press. Published by Elsevier B.V. and Science China Press. All rights are reserved, including those for text and data mining, Al training, and similar technologies.

1. Introduction

Although most quantum-mechanical phenomena are observed by isolating the quantum systems from their surrounding environment so as to minimize the decoherence effects arising from interaction with the environment, the non–Hermitian (NH) effects due to dissipations can sometimes cause novel features that are inaccessible otherwise [1–4]. The rich physics of non–Hermitian systems is closely associated with exceptional points (EPs), featuring the coalescence of both the eigenenergies and eigenstates. This enables EPs to display distinct properties compared to the degeneracies of Hermitian systems, where the eigenenergies coalesce but the eigenstates can remain orthogonal. Among these, exceptional topology is particularly appealing, which can manifest in either the eigenspectra or in the eigenvectors of the NH Hamiltonian [5,6]. The topological invariants of isolated EPs have been measured in different systems [7–15].

The topology features associated with non-Hermiticity are further enriched by the discovery of one- and two-dimensional (2D) EP structures, such as EP rings [16-26] and EP surfaces [27,28]. When some control parameter in the Hamiltonian is extended from the real domain to the complex domain, each EP pair is transformed into a ring, referred to as the Weyl exceptional ring (WER). It was discovered that a WER formed by second-order EPs (EP2s) carries a quantized Berry charge, which can be characterized by a Chern number obtained by integrating the Berry curvature over a closed 2D surface encompassing the ring, as well as by a quantized Berry phase associated with the integral of the Berry connection along a loop encircling the ring [17]. WERs have been observed in several experiments [22-26], but all are restricted to classical systems without any quantum effect. Even for the classical implementations, the associated Chern number has not been observed so far.

We here investigate the topological transition associated with the WER encoded in the entangled eigenvectors of a dissipative Jaynes-Cummings (JC) model. This model consists of a qubit and a decaying resonator, engineered with a circuit quantum electrodynamics (QED) architecture. One of the superconducting qubits in the circuit QED device is coupled to its readout resonator with an ac flux that pro-

a Fujian Key Laboratory of Quantum Information and Quantum Optics, College of Physics and Information Engineering, Fuzhou University, Fuzhou 350108, China

^b School of Physics and Mechanical and Electrical Engineering, Longyan University, Longyan 364012, China

^c School of Physics, Hangzhou Normal University, Hangzhou 311121, China

^d Hefei National Laboratory, Hefei 230088, China

^{*} Corresponding authors.

E-mail addresses: ningw@fzu.edu.cn (W. Ning), zbyang@fzu.edu.cn (Z.-B. Yang), t96034@fzu.edu.cn (S.-B. Zheng)

¹ These authors contributed equally to this work.

duces a longitudinal parametric modulation to the qubit's transition frequency. The effective qubit-resonator coupling strength and detuning are tunable by the modulation amplitude and frequency. In the absence of dissipation, the Berry topological charge is carried by the degeneracy of the qubit-boson entangled eigenstates, which resides at the origin of the parameter space. The dissipation extends the point-like singularity to a ring, realizing a WER in the parameter space. The Berry curvature, which serves as a fictitious magnetic field, is extracted from the eigenvectors measured for different settings of the control parameter. By reducing the size of the loop (manifold) so as not to encircle (enclose) the WER, the system undergoes a topological transition, manifested by an abrupt change of the Berry phase (Chern number).

2. Model and methods

We first consider the topology encoded in the parameter space of the JC model without dissipation (Fig. 1a). In the framework rotating at the frequency of the resonator, the system Hamiltonian is given by (setting h = 1) [29,30]

$$H_{S} = \Delta |e\rangle \langle e| + \lambda a^{\dagger} |g\rangle \langle e| + \lambda^{*} a |e\rangle \langle g|, \tag{1}$$

where $|e\rangle$ and $|g\rangle$ are the upper and lower levels of the qubit, a^{\dagger} and a are the creation and annihilation operators for the quantized field stored in the resonator, and λ and Δ denote the qubit-cavity coupling coefficient and detuning, respectively. In the singleexcitation subspace, the composite qubit-resonator system can be taken as a spin, with the basis states $|e,0\rangle$ and $|g,1\rangle$ respectively corresponding to the spin-up and -down states $|\uparrow\rangle$ and $|\downarrow\rangle$, where the number in each ket denotes the photon number of the resonator. With this analogy, the system dynamics can be described as the motion of the spin in a magnetic field B with the components $B_x = \text{Re}(\lambda), B_y = \text{Im}(\lambda)$, and $B_z = \Delta/2$, as shown in Fig. 1b. This Hermitian system has a degeneracy at the origin, referred to as a diabolic point, where the two eigenenergies coalesce but the eigenvectors do not. This degeneracy is a mathematic analog of the magnetic monopole that carries a quantized topological charge in the parameter space, as shown in Fig. 1c. Due to the presence of such a topological defect, any manifold that encloses this singularity in the parameter space is topologically distinct from those without involving it. The fictitious magnetic field emanated from the topological charge is manifested by the Berry curvature. The quantized Berry flux penetrating through the manifold is characterized by the Chern number, defined as the integral of the Berry curvature over the manifold.

With the dissipation of the photonic field being included, the system dynamics is described by a master equation. Conditional

upon no photon being leaked into the environment, the system dynamics is described by the NH Hamiltonian [31–34]

$$H_{\rm NH} = H_{\rm S} - \frac{1}{2}i\kappa a^{\dagger}a,\tag{2}$$

with κ being the decaying rate of the photonic field. The eigenvectors of the NH Hamiltonian are drastically different from those of its Hermitian counterpart. Due to the non–Hermiticity, the left and right eigenvectors, defined as $H_{\rm NH}|u_n^r\rangle=E_n|u_n^r\rangle$ and $\langle u_n^l|H_{\rm NH}=\langle u_n^l|E_n\rangle$, are not the Hermitian conjugates of each other, and need to be obtained separately. For the present NH Hamiltonian, the two non-orthogonal right eigenvectors, $|u_n^r\rangle$ (n=1,2), in the single-excitation subspace can be written as

$$\left|u_{n}^{r}\right\rangle = \frac{\lambda^{*}|e,0\rangle + (E_{n} - \Delta)|g,1\rangle}{\sqrt{\left|\lambda\right|^{2} + \left|E_{n} - \Delta\right|^{2}}},\tag{3}$$

where

$$E_{1,2} = \frac{2\Delta - i\kappa}{4} \pm \sqrt{\left|\lambda\right|^2 + \frac{\left(2\Delta + i\kappa\right)^2}{16}}.$$
 (4)

The left eigenvectors can be obtained from the biorthonormal condition [5,6]:

$$\langle u_n^l | u_m^r \rangle = \delta_{m,n}. \tag{5}$$

The non–Hermiticity changes the point-like degeneracy into a WER with the radius of $B_{\rm WER}=\kappa/4$, centered at the origin and located on the B_x - B_y plane of the parameter space (Fig. 1d). Along the WER, both the eigenenergies and eigenvectors coalesce. Due to the ring-like structure of the topological defect, the topology of the parameter-space manifold depends upon its position, as well as upon its size, which is fundamentally distinct from that of a Hermitian system.

3. Results

We engineer the WER and demonstrate its topological feature using a circuit QED device with a bus resonator (R_b) and 5 frequency-tunable qubits, one of which (Q), together with its readout resonator (R), is used to realize the spin-boson model. Q has an energy relaxation time $T_1 \approx 14.3~\mu s$ and a pure Gaussian dephasing time $T_2^* \approx 5.3~\mu s$ at its idle frequency $\omega_I/2\pi = 6.0~\text{GHz}$, where it is transformed from the initial ground state $|g\rangle$ to the excited state $|e\rangle$ with a π pulse. During application of the pulse, Q is highly detuned and thus effectively decoupled from both R_b and R with frequencies $\omega_b/2\pi = 5.584~\text{GHz}$ and $\omega/2\pi = 6.656~\text{GHz}$, respectively. The pulse sequence is sketched in the Supplemental

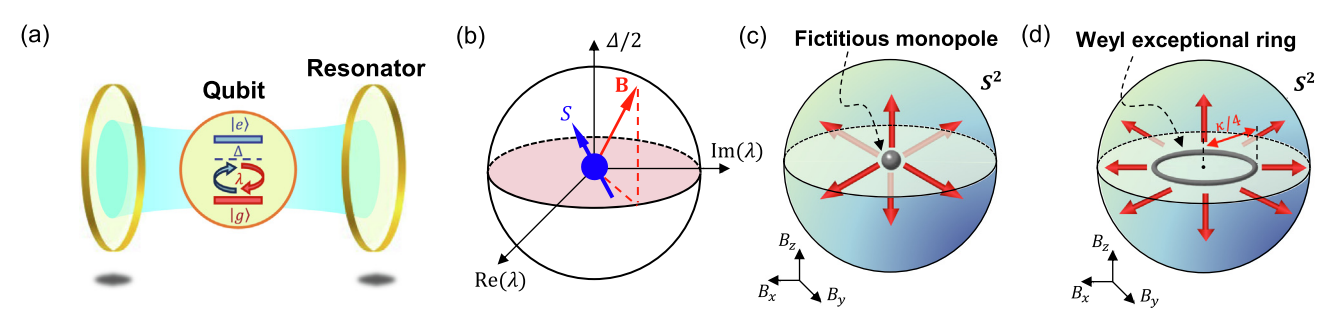


Fig. 1. Construction of the WER. (a) The JC model. The system is composed of a photonic mode stored in a resonator interacting with a qubit, whose upper and lower levels are respectively denoted as $|e\rangle$ and $|g\rangle$. The qubit-resonator coupling coefficient and detuning are λ and Δ , respectively. (b) Spin representation. In the single-excitation subspace $\{|\uparrow\rangle \equiv |e,0\rangle, |\downarrow\rangle \equiv |g,1\rangle\}$, the dynamics of the composite system is mathematically equivalent to a spin-1/2 (5) moving in a magnetic field **B**, whose x-, y-, and z-components correspond to Re(λ), Im(λ), and Δ /2, respectively. (c) Point-like topological defect. In the absence of dissipation, the eigenspectrum displays a twofold degeneracy at the origin of the 3D parameter space $\{B_x, B_y, B_z\}$, which can be considered as a fictitious monopole carrying a quantized topological charge. (d) WER. The non–Hermiticity is manifested by the photonic dissipation of the resonator with a rate κ . Due to the presence of dissipation, the point-like singularity is extended to a ring with the radius of $B_{WER} = \kappa/4$, centered at the origin and located on the B_x - B_y plane of the parameter space.

Material. After this transformation, Q is coupled to R through application of an ac flux, modulating the qubit frequency as $\omega_a = \omega_0 + \varepsilon \cos(vt)$ [4], where ω_0 is the mean frequency and $\varepsilon(v)$ is the modulation amplitude (frequency), respectively. The modulation frequency $v \approx 2\pi \times$ (678.4–643.0) MHz is close to $\omega - \omega_0$, so that Q is quasi-resonantly coupled to R at the first upper sideband of the modulation. The couplings at the carrier and other sidebands can be discarded due to large detunings. The system evolution is approximately governed by the Hamiltonian of Eq. (1) with the effective coupling $\lambda = \lambda_r J_1(\mu)$ and the detuning $\Delta = v + \omega_0 - \omega$, where $\mu = \varepsilon/v$, $J_1(\mu)$ is the first-order Bessel function of the first kind, and $\lambda_r = 2\pi \times 41$ MHz denotes the onresonance coupling strength between the qubit and the readout resonator. The Hamiltonian parameters Δ and λ are tunable by the parametric modulation pulse, and the non-Hermiticity is manifested by the photonic dissipation with a rate of $\kappa = 5$ MHz. The decaying rates of Q and R_h , 0.07 and 0.083 MHz, are much smaller than κ , and thus can be discarded. As R is initially in the vacuum state, the Q-R system evolves in the single-excitation subspace, so that both the qubit and the resonator cannot be coupled to energy levels with more than one excitation during their interaction.

The topological features of the engineered WER are manifested by the quantized Berry phase acquired along a loop encircling it, as well as by the Chern number associated with a manifold enclosing it. The Berry phase is defined as [16]

$$\beta_n = i \oint_{\partial \mathcal{L}} \langle u_n^l(\mathbf{B}) | \frac{\partial}{\partial \mathbf{B}} | u_n^r(\mathbf{B}) \rangle \cdot d\mathbf{B}, \tag{6}$$

where the path $2\mathcal{L}$ travels across the ring twice along the loop in parameter space (Fig. 2a), so that the eigenvector returns to the original one after the entire trajectory. When the loop encircles the WER, the acquired Berry phase is $\pm \pi$, which becomes zero for a loop without encircling it. Due to the chiral nature associated with the non–Hermiticity, the system does not adiabatically follow a specific eigenvector by slowly changing the control parameter [35]. The breakdown of the adiabaticity prevents measurement of the Berry phase by adiabatic evolution. However, the Berry phase associated with each eigenvector is encoded in the parameter space, and has no direct relation to the evolution time. This enables us to infer the Berry phase

by measuring the dependence of the eigenvector on the control parameter [4], without resorting to the adiabatic process.

The eigenvectors for a preset control parameter can be extracted from the joint Q-R output states dynamically evolved for different times under the NH Hamiltonian of Eq. (2). The interaction time is controlled by the parametric modulating pulse. When the modulation is switched off, Q is effectively decoupled from R due to large detuning. Then Q's state is mapped to an ancilla qubit Q_a with the assistance of R_b , following which R's state is transferred to Q through the modulation-induced sideband interaction. The resulting joint Q_a -Q state projected to the singleexcitation subspace, which can be measured by the quantum state tomography and postselection technique [4], corresponds to the Q-R output state just before the state transfer procedure. The eigenvectors are inferred from the tracked time-evolving Q-R output states, as detailed in the Supplemental Material. We choose circular loops centered at $(B_z = 0, B_x = \kappa/2)$ on the B_x - B_z plane. With this choice, whether or not the WER is encircled depends on the radius of the traversed loop (B_r) , as shown in Fig. 2a. We can fit right eigenvectors $|u_n^r(\mathbf{B})\rangle$ as functions of the control parameter **B** with the results extracted for different settings of B, and calculate the left vectors $|u_n^l(\mathbf{B})\rangle$ using the biorthonormal condition, Fig. 2b shows the Berry phase (β_1 and β_2) for the two pairs of eigenvectors versus B_r . These Berry phases, measured at $B_r = 0.427\kappa$, are about -0.9844π and -0.9844π , respectively. With the shrinking of the loop, each of these Berry phases makes an abrupt change around $B_r = 0.226\kappa$, quickly dropping to 0 when crossing this critical point, thereby manifesting a topological transition. Owing to control errors, such an experimentally inferred critical point slightly deviates from the theoretical value $\kappa/4$. We note that it is experimentally challenging to extract the eigenstates when the control parameter is infinitely close to the critical point. This is due to the fact that both the eigenstates and eigenenergies tends to coalesce, so that the state evolution speeds become infinitely slow in this case. Consequently, the jump of the Berry phase from $-\pi$ to 0 at the critical point cannot be unambiguously confirmed. In our experiment, the minimum (maximal) value of B_r for the observed trivial (topological) phase is 0.126κ (0.427κ).

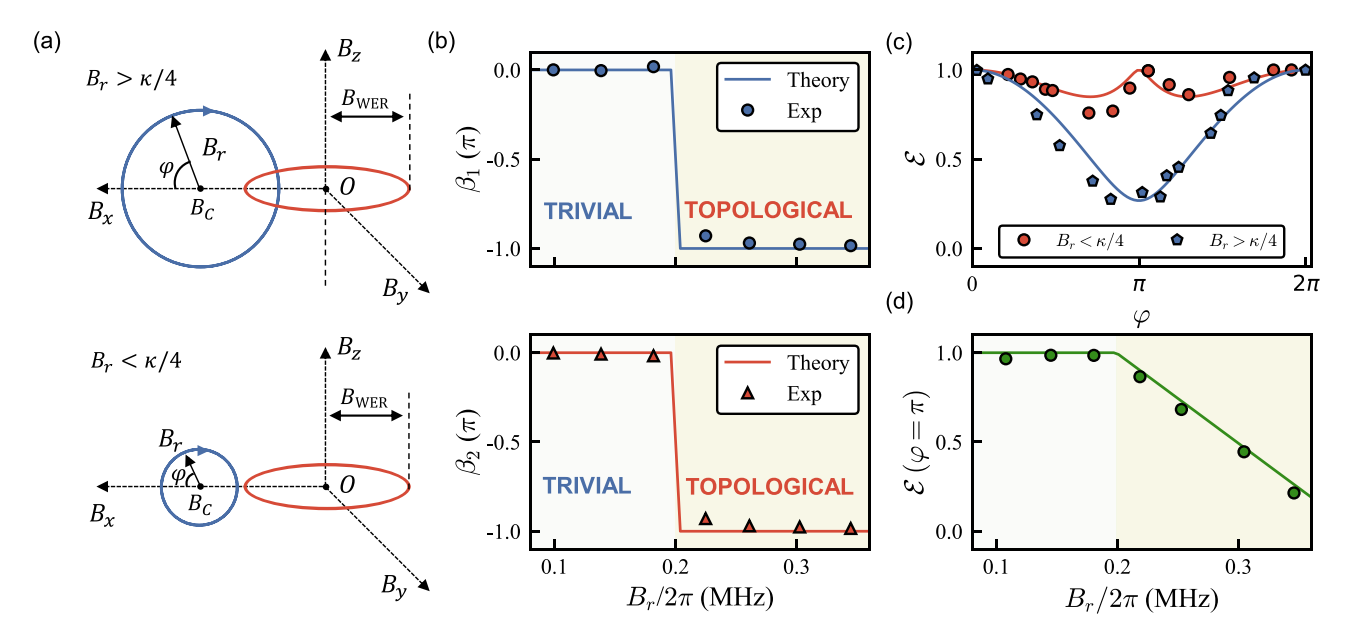


Fig. 2. Topological transition characterized with the Berry phase. (a) Loops associated with topologically distinct phases. The loops are circularly-shaped, and centered at $(B_x = \kappa/2, B_z = 0)$ on the B_x - B_z plane. The WER is encircled when the radius of the traversed loop (B_r) is in the range $(\kappa/4, 3\kappa/4)$. (b) Measured Berry phase versus B_r . β_1 and β_2 denote the results associated with the two pairs of eigenvectors $\{|u_n^r(\mathbf{B})\rangle, |u_n^l(\mathbf{B})\rangle\}$ with n = 1, 2. (c) Measured qubit-resonator concurrences (\mathcal{E}) versus φ for different values of B_r $(B_r/2\pi = 0.18, 0.34 \text{ MHz})$. At each point, the concurrences are obtained from the corresponding right eigenvectors. (d) $\mathcal{E}(\pi)$ versus B_r .

Unlike previous implementations of WERs [5,6,22,23,25], in our system the topological characteristic is encoded in highly nonclassical states of the joint Q-R system. In the single-excitation subspace, the quantum entanglement between Q and R can be well measured by the concurrence \mathcal{E} [36]. The concurrences of each right eigenvector versus φ for different values of B_r are presented in Fig. 2c, where φ is the angle between the control parameter **B** and the x-axis in the displaced frame, whose origin coincides with the center of the loops. The solid lines denote the results for the ideal eigenvectors. We note that the topological phase transition is closely related to the exceptional entanglement behavior. When $B_r < B_C - B_{WER} = \kappa/4$, the system works above the EP where $B_x = \kappa/4$ and $B_y = B_z = 0$ for both $\varphi = 0$ and π , and consequently $\mathcal{E}(0) = \mathcal{E}(\pi) = 1$ in theory [4]. Here $B_C = \kappa/2$ denotes the magnitude of **B** at the center of the loops. For $B_r > \kappa/4$, $\mathcal{E}(0) = 1$, while $\mathcal{E}(\pi)$ linearly increases with $B_C - B_r$. This implies that $\mathcal{E}(\pi)$ is independent of B_r for the trivial phase, but exhibits a B_r -dependence for the topological phase. To confirm this point, in Fig. 2d, we display the measured $\mathcal{E}(\pi)$ versus B_r , which is well agreement with the ideal result (solid line). Consequently, the derivative of $\mathcal{E}(\pi)$ with respect to B_r is not continuous at the point $B_r = \kappa/4$ [4]. These results clearly demonstrate that the geometric features of the system are encoded in the entangled states of Q and R, illustrating the quantum-mechanical character of the measured Berry phase, and the topological phase transition coincides with the exceptional entanglement phase transition [4].

It is convenient to calculate the Chern number on a spherical manifold, which is centered at the origin of the parameter space. For a sphere with a specific radius B_r , the control parameters are the polar and azimuth angles (θ,ϕ) . The ϕ and θ components of the Berry connection are defined as

$$A_{\phi}^{n} = i \langle u_{n}^{r}(\theta, \phi) | \partial_{\phi} | u_{n}^{r}(\theta, \phi) \rangle,$$

$$A_{\theta}^{n} = i \langle u_{n}^{r}(\theta, \phi) | \partial_{\theta} | u_{n}^{r}(\theta, \phi) \rangle.$$

$$(7)$$

The Chern number is given by

$$C_n = \frac{1}{2\pi} \int_0^{2\pi} d\phi \int_0^{\pi} d\theta F_{\theta\phi}^n, \tag{8}$$

where $F_{\theta\phi}^n = \partial_\theta A_\phi^n - \partial_\phi A_\theta^n$ denotes the Berry curvature [16,37,38]. When $B_r > \kappa/4$, the WER is enclosed in the manifold (Fig. 3a), so that the quantized Berry flux emanated from the WER pierces through the manifold, and the Chern number is ± 1 . For $B_r < \kappa/4$, the sphere is located inside the ring (Fig. 3b), the Berry flux entering the manifold and that going out of it cancel out each other, resulting in a zero Chern number.

Due to the spherical symmetry, the Berry connection A^n_{θ} is independent of ϕ , so that $F^n_{\theta\phi}=\partial_{\theta}A^n_{\phi}$. Taking advantage of this symmetry, the Chern number can be obtained from the results measured along 0° -meridian [39,40],

$$C_n = \int_0^{\pi} d\theta \partial_{\theta} A_{\phi}^n = P_{e,0}^n(\pi) - P_{e,0}^n(0), \tag{9}$$

where $P_{e,0}^n(\theta)$ is the population of $|e,0\rangle$ in the eigenvector $|u_n^r(\theta,0)\rangle$. With data of $P_{e,0}^n$ measured for different values of θ , we can fit the function $P_{e,0}^n(\theta)$, which are shown in Fig. 3c and d. In our experiment, it is difficult to extract the eigenvectors when λ is equal to 0 (see Supplemental Material for details). Here we calculate the Chern number using the measured values of $P_{e,0}^{n}(\theta_1)$ and $P_{e,0}^{n}(\theta_2)$, where θ_1 and θ_2 are as close to π and 0 as possible, respectively. Fig. 3e displays thus-obtained Chern numbers C_1 and C_2 versus the radius of the manifold. As expected, the Chern numbers, measured on a manifold with a radius larger than that of the WER $\kappa/4$, are equal to ± 1 . When B_r is reduced to the critical value of $\kappa/4$, a topological transition occurs, characterized by an abrupt drop of the Chern number to 0. These results can be interpreted as follows. Under the condition that the WER is enclosed in the manifold, the eigenvector $|u_n^r(\theta, 0)\rangle$ makes a π rotation, flipping from $|g,1\rangle(|e,0\rangle)$ to $|e,0\rangle(|g,1\rangle)$ following the variation of θ from 0 to π , as illustrated in Fig. 3c, where $B_r/2\pi = 0.33$ MHz. In distinct contrast, for $B_r < \kappa/4, |u_n^r(\theta,0)\rangle$ tilts away from vertical with an angle smaller than $\pi/2$ and then returns (Fig. 3d, $B_r/2\pi = 0.18$ MHz). The measured $P_{e,0}^n$ versus θ for different values of B_r are detailed in Supplemental Material. We note this topological behavior represents a unique characteristic that distinguishes the NH system from Hermitian ones, where a topological transition occurs only when the manifold is displaced so as not to

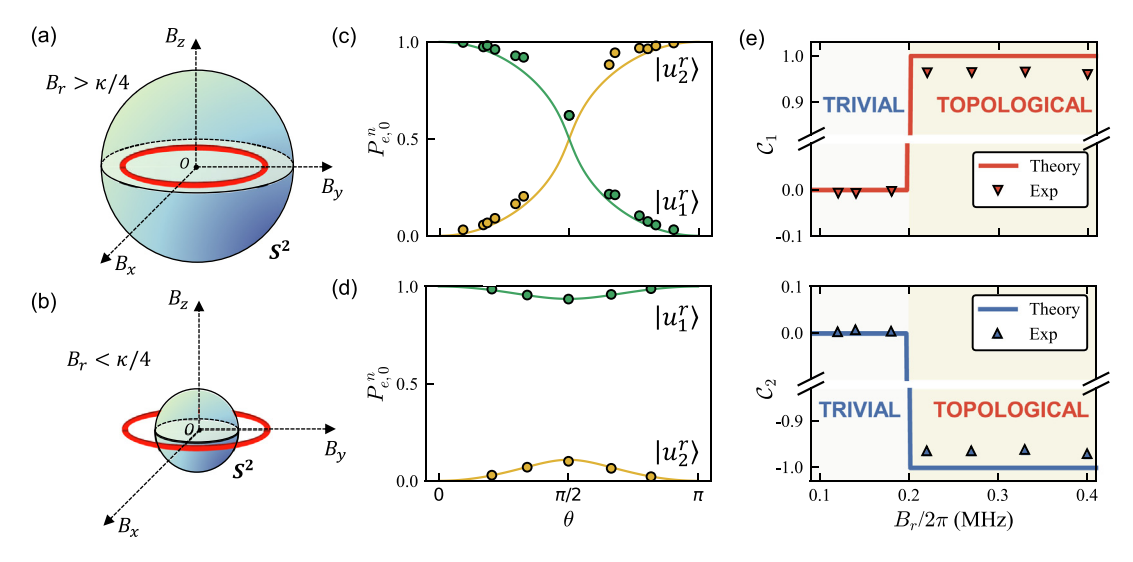


Fig. 3. Topological transition characterized with Chern number. (a, b) Manifolds associated with topologically distinct phases. The spherical manifolds are centered at the origin of the 3D parameter space. When the WER is enclosed in the manifold (a), the quantized Berry flux emanated from the WER pierces through the manifold. When the sphere is located inside the ring (b), the amount of the Berry flux entering the manifold equals the amount going out of it. (c, d) Measured populations of $|e,0\rangle$ in $|u_n^r(\theta,\phi)\rangle(n=1,2)$ versus θ for $B_r/2\pi=0.33$ MHz (c) and 0.14 MHz (d). Here (B_r,θ,ϕ) denote the spherical coordinates for the control parameter. All data are measured for $\phi=0$. The lines denote the functions fitted with the measured data. (e) Measured Chern number versus the radius of the manifold. C_1 and C_2 denote the results associated with the two right eigenvectors $|u_1^r(B)\rangle$ and $|u_2^r(B)\rangle$, respectively.

enclose the origin of parameter space—the diabolic point [9,15,39–45], but cannot be realized by shrinking the manifold centered at the diabolic point. Because of the experimental limitation, the minimum (maximal) value of B_r for the observed trivial (topological) phase is 0.151κ (0.503κ).

4. Discussion and conclusion

In conclusion, we have constructed a WER in a system composed of a qubit coupled to a resonator supporting a decaying photonic field, and characterized its topological features by the quantized Berry phase and Chern number, which are inferred from the measured eigenvectors of the governing NH Hamiltonian. We have observed a topological phase transition featuring a change of the Chern numbers from ± 1 to 0, by continually reducing the size of the spherical manifold centered at the origin of the parameter space. Our results confirm that the non–Hermiticity changes a point-like degeneracy into a 2D ring of EPs, giving arise to exceptional topological phenomena that are absent in Hermitian systems. Our method can be generalized to realize the EP ring associated with a non-Abelian monopole and to explore NH topological transitions based on a higher-order Chern number.

Conflict of interest

The authors declare that they have no conflict of interest.

Acknowledgments

This work was supported by the National Natural Science Foundation of China (12274080, 12474356, 12475015, and U21A20436) and Innovation Program for Quantum Science and Technology (2021ZD0300200 and 2021ZD0301705).

Author contributions

Shi-Biao Zheng conceived the experiment. Wen Ning, Hao-Long Zhang, and Pei-Rong Han supervised by Zhen-Biao Yang and Shi-Biao Zheng, carried out the experiment. Hao-Long Zhang, Pei-Rong Han, and Xue-Jia Yu analyzed the data. Shi-Biao Zheng, Zhen-Biao Yang, and Xue-Jia Yu co-wrote the paper. Shou-Bang Yang, Jia-Hao Lü, Fan Wu, Qi-Ping Su, and Chui-Ping Yang helped to interpret the observed phenomena and to write the paper.

Appendix A. Supplementary material

Supplementary data to this article can be found online at https://doi.org/10.1016/j.scib.2025.05.041.

References

- [1] Bender CM, Brody DC, Jones HF. Complex extension of quantum mechanics. Phys Rev Lett 2002;89:270401.
- [2] Miri MA, Andrea A. Exceptional points in optics and photonics. Science 2019;363:7709.
- [3] Özdemir ŞK, Rotter S, Nori F, et al. Parity-time symmetry and exceptional points in photonics. Nat Mater 2019;18:783–98.
- [4] Han PR, Wu F, Huang XJ, et al. Exceptional entanglement phenomena: non-Hermiticity meeting nonclassicality. Phys Rev Lett 2023;131:260201.
- [5] Bergholtz EJ, Budich JC, Kunst FK. Exceptional topology of non-Hermitian systems. Rev Mod Phys 2021;93:015005.
- [6] Ding K, Fang C, Ma GC. Non-Hermitian topology and exceptional-point geometries. Nat Rev Phys 2022;4:745–60.
- [7] Zhou HY, Chao P, Yoon Y, et al. Observation of bulk Fermi arc and polarization half charge from paired exceptional points. Science 2018;359:1009–12.
- [8] Su R, Estrecho E, Biegańska D, et al. Direct measurement of a non-Hermitian topological invariant in a hybrid light-matter system. Sci Adv 2021;7:
- [9] Tang W, Ding K, Ma G. Direct measurement of topological properties of an exceptional parabola. Phys Rev Lett 2021;127:034301.

[10] Zhang W, Ouyang X, Huang X, et al. Observation of non-Hermitian topology with nonunitary dynamics of solid-state spins. Phys Rev Lett 2021:127:090501.

- [11] Wang K, Dutt A, Yang KY, et al. Generating arbitrary topological windings of a non-Hermitian band. Science 2021;371:1240–5.
- [12] Zhang QC, Li Y, Sun H, et al. Observation of acoustic non-Hermitian bloch braids and associated topological phase transitions. Phys Rev Lett 2023;130:017201.
- [13] Cao MM, Li K, Zhao WD, et al. Probing complex-energy topology via non-Hermitian absorption spectroscopy in a trapped ion simulator. Phys Rev Lett 2023:130:163001.
- [14] Wu Y, Wang YH, Ye XY, et al. Observation of the knot topology of non-Hermitian systems in a single spin. Phys Rev A 2023;108:052409.
- [15] Han PR, Ning W, Huang XJ, et al. Measuring topological invariants for higherorder exceptional points in quantum three-mode systems. Nat Commun 2024;15:10293.
- [16] Xu Y, Wang ST, Duan LM. Weyl exceptional rings in a three-dimensional dissipative cold atomic gas. Phys Rev Lett 2017;118:045701.
- [17] Yoshida T, Peters R, Kawakami N, et al. Symmetry-protected exceptional rings in two-dimensional correlated systems with chiral symmetry. Phys Rev B 2019;99:121101–R.
- [18] Liu T, He JJ, Yang Z, et al. Higher-order Weyl-exceptional-ring semimetals. Phys Rev Lett 2021;127:196801.
- [19] Ghorashi SAA, Li T, Sato M. Non-Hermitian higher-order Weyl semimetals. Phys Rev B 2021;104:L161117.
- [20] Mc Guinness RL, Eastham PR. Weyl points and exceptional rings with polaritons in bulk semiconductors. Phys Rev Res 2020;2:043268.
- [21] Matsushita T, Nagai Y, Fujimoto S. Disorder-induced exceptional and hybrid point rings in Weyl/Dirac semimetals. Phys Rev B 2019;100:245205.
- [22] Zhen B, Hsu CW, Igarashi Y, et al. Spawning rings of exceptional points out of Dirac cones. Nature 2015;525:354–8.
- [23] Cerjan A, Huang S, Wang M, et al. Experimental realization of a Weyl exceptional ring. Nat Photonics 2019;13:623–8.
- [24] Tang W, Jiang X, Ding K, et al. Exceptional nexus with a hybrid topological invariant. Science 2020;370:1077–80.
- [25] Liu JJ, Li ZW, Chen ZG, et al. Experimental realization of Weyl exceptional rings in a synthetic three-dimensional non-Hermitian phononic crystal. Phys Rev Lett 2022;129:084301.
- [26] Tang W, Ding K, Ma GC. Realization and topological properties of third-order exceptional lines embedded in exceptional surfaces. Nat Commun 2023;14:6660.
- [27] Zhang X, Ding K, Zhou X, et al. Experimental observation of an exceptional surface in synthetic dimensions with magnon polaritons. Phys Rev Lett 2019;123:237202.
- [28] Zhou H, Lee JY, Liu S, et al. Exceptional surfaces in PT-symmetric non-Hermitian photonic systems. Optica 2019;6:190–3.
- [29] Jaynes ET, Cummings FW. Comparison of quantum and semiclassical radiation theories with application to the beam maser. Proc IEEE 1963;51:89–109.
- [30] Shore BW, Knight PL. The Jaynes-Cummings model. J Mod Opt 1993;40:1195–238.
- [31] Scala M, Militello B, Messina A, et al. Cavity losses for the dissipative Jaynes-Cummings Hamiltonian beyond rotating wave approximation. J Phys A: Math Theor 2007;40:14527.
- [32] Fujii K, Suzuki T. An approximate solution of the Jaynes-Cummings model with dissipation. Int | Geom Methods Mod Phys 2011;8:1799–814.
- [33] Li HC, Xiong W, Ge GQ, et al. Universal zeno competition in the dissipative Jaynes-Cummings model. Phys Rev A 2022;105:052208.
- [34] Viotti L, Lombardo FC, Villar PI. Geometric phase in a dissipative Jaynes-Cummings model: theoretical explanation for resonance robustness. Phys Rev A 2022:105:022218.
- [35] Zhang XL, Wang S, Hou B, et al. Dynamically encircling exceptional points: in situ control of encircling loops and the role of the starting point. Phys Rev X 2018:8:021066.
- [36] Wootters WK. Entanglement of formation of an arbitrary state of two qubits. Phys Rev Lett 1998;80:2245–8.
- [37] Berry MV. Quantal phase factors accompanying adiabatic changes. Proc R Soc Lond A 1984;392:45–57.
- [38] Yin X, Chen Y, Zhang X, et al. Observation of Berry curvature in non-Hermitian system from far-field radiation. Nat Commun 2025;16:2796.
- [39] Schroer MD, Kolodrubetz MH, Kindel WF, et al. Measuring a topological transition in an artificial spin-1/2 system. Phys Rev Lett 2014;113:050402.
- [40] Jotzu G, Messer M, Desbuquois R, et al. Experimental realization of the topological Haldane model with ultracold fermions. Nature 2014;515:237–40.
- [41] Tan X, Zhang DW, Yang Z, et al. Experimental measurement of the quantum metric tensor and related topological phase transition with a superconducting qubit. Phys Rev Lett 2019;122:210401.
- [42] Sugawa S, Salces-Carcoba F, Perry AR, et al. Second chern number of a quantum-simulated non-Abelian Yang monopole. Science 2018;360: 1429–34.
- [43] Tan X, Zhang DW, Zheng W, et al. Experimental observation of tensor monopoles with a superconducting qudit. Phys Rev Lett 2021;126:017702.
- [44] Chen M, Li CH, Palumbo G, et al. A synthetic monopole source of Kalb-Ramond field in diamond. Science 2022;375:1017–20.
- [45] Yu M, Yang P, Gong M, et al. Experimental measurement of the quantum geometric tensor using coupled qubits in diamond. Nat Sci Rev 2019;7:254–60.